UDK 669.14.018.8:001.124
Original scientific article/Izvirni znanstveni članek

ISSN 1580-2949
Mater. Tehnol.

DEVELOPMENT OF FERRITE-CONTENT CONTROL PROCESS FOR 316LN AUSTENITIC STAINLESS STEEL FOR LIQUID-HYDROGEN STORAGE BASED ON HIGH-FLUX PREPARATION

RAZVOJ PROCESA KONTROLE VSEBNOSTI DELTA FERITA V MIKROSTRUKTURI AUSTENITNEGA NERJAVNEGA JEKLA TIPA 316LN, UPORABNEGA ZA SHRANJEVANJE VELIKIH KOLIČIN TEKOČEGA VODIKA

Xin Ouyang[1,2], Xuemin Wang[1]*, Chenxi Liu[2,3], Mengnan Xing[2,3], Yunfeng Bai[2,3], Xinming Hu[2,3]

[1]Collaborative Innovation Center of Steel Technology, University of Science and Technology Beijing, Beijing 100083, PR China
[2]State Key Laboratory of Metallic Materials for Marine Equipment and Applications, Anshan, Liaoning 114009, PR China
[3]Iron and Steel Research Institute of Ansteel Group, Anshan, Liaoning 114009, PR China

Prejem rokopisa – received: 2025-03-20; sprejem za objavo – accepted for publication: 2025-06-04

doi:10.17222/mit.2025.1425

Designing multiple alloy compositions to achieve target performance is the first step in modern new-material development, but traditional trial-and-error experiments severely hinder progress due to their low efficiency. This article proposes the use of a multi-crucible synchronous metallurgy method in high-throughput experiments to accelerate the composition design of 316LN austenitic stainless steel for liquid hydrogen storage. Twenty as-cast samples of austenitic stainless steel with different compositions were prepared using a high-throughput material preparation system through two rounds of experiments. Then, through microscopic observation and mechanical property testing, the chemical composition that best matched the target performance was ultimately selected. The research results indicate that high-throughput experiments can greatly improve the efficiency of optimizing the composition design of new stainless steel products. Meanwhile, this investigation also analyzed the precipitation of δ-ferrite in austenitic stainless steel and proposed effective methods for controlling the content of δ-ferrite. The high-temperature δ-ferrite in 316H stainless steel originates from the solidification process. Due to the redistribution of elements during solidification, Cr and Mo tend to segregate at dendrites or grain boundaries, forming regions enriched in these elements, resulting in the nucleation and growth of ferrite. This investigation uses a metallographic microscope, electron probe, EBSD and other methods to study the distribution of Cr, Mo and other elements in the microstructure of 316LN stainless steel, observe the evolution morphology of different microstructures, as well as explore how ferrite content changes with chemical composition and production process. It was ultimately determined that high-temperature and long-term sensitization treatment is an effective method to control the content of δ-ferrite.

Keywords: high-throughput preparation, austenitic stainless steel, δ-ferrite, sensitization heat treatment, galvanic corrosion

Dizajn (načrtovanje) večkomponentnih zlitin je prvi korak pri sodobnem razvoju novih materialov. Tradicionalni pristop z metodo *preizkusa in napake* (angl.: trial and error experiments) zaradi svoje nizke učinkovitosti močno omejuje napredek razvoja novih materialov. V tem članku avtorji predlagajo uporabo metode sinhrone metalurgije z več talilnimi lončki. Takšni preizkusi so učinkovitejši in močno pospešijo načrtovanja optimalne sestave nove zlitine. V tem primeru austenitnega nerjavnega jekla tipa 316LN za shranjevanje tekočega vodika. Avtorji so istočasno pripravili v dveh krogih (»rundah«) dvajset (20) ulitih vzorcev austenitnega nerjavnega jekla z različnimi kemijskimi sestavami. Nato so z metalografskim opazovanjem in določitvijo mehanskih lastnosti preizkušancev končno izbrali kemično sestavo jekla, ki je najbolj ustrezala zahtevanim parametrom. Rezultati raziskave so pokazali, da so izvedeni preizkusi močno povečali učinkovitost optimizacije načrtovanja kemijske sestave novega nerjavnega jekla. V okviru raziskave so avtorji analizirali tudi proces izločanjaa d-ferita v austenitnem nerjavnem jeklu in določili učinkovito metode za nadzor vsebnosti le-te. Visokotemperaturni d-ferit v nerjavnem jeklu 316LN nastaja med procesom strjevanja. Zaradi prerazporeditve kemijskih elementov med procesom strjevanja zlitinska elementa Cr in Mo zlahka difundirata in obogatita področja dendritov ali mej kristalnih zrn. S tem nastanejo območja s povečano koncentracijo Cr in Mo, kar povzroči nukleacijo in rast d-ferita. Avtorji so za raziskave in karakterizacijo zlitin uporabljali metalografski mikroskop, elektronsko mikro sondo, vrstični elektronski mikroskop (SEM) s spektroskopijo sipanja povratnih elelktronov (EBSD; Electron Backscatter Diffraction) in druge metode za preučevanje porazdelitve Cr, Mo in drugih elementov v mikrostrukturi preiskovanega nerjavnega jekla 316LN. Avtorji v zaključkih članka poudarjajo, da so visokotemperaturna in dolgotrajna senzibilizacijska toplotna obdelava, opazovanje morfologije razvoja in nastanka različnih mikrostruktur, raziskovanje zakonov spreminjanja vsebnosti ferita s kemično sestavo in proizvodnim procesom učinkovite metode za nadzor vsebnosti d-ferita.

Ključne besede: visokozmogljiva priprava, austenitno nerjavno jeklo, d-ferit, senzibilizacijska toplotna obdelava, galvanska korozija

---

*Corresponding author's e-mail:
wxm@mater.ustb.edu.cn (Xuemin Wang)

1 INTRODUCTION

Under the environmental trend of carbon neutrality and peak carbon emissions, the importance of hydrogen energy has been widely recognized. In recent years, the entire industry chain for hydrogen production, storage, transportation, and application has achieved rapid development. The storage and transportation technology of hydrogen, as a key link in the production and practical application of hydrogen, has become an important support for the safety and efficiency of hydrogen energy applications. With the continuous expansion and popularization of hydrogen energy applications, large-scale hydrogen storage and transportation technology will also usher in opportunities for rapid development. Among them, the low-temperature liquid hydrogen storage and transportation method is highly likely to become the main choice for large-scale hydrogen storage and transportation in the civilian field as it allows high storage and transportation density and low cost of long-distance transportation.[1,2] This research combines high-throughput experiments with microstructure observation to develop a new type of liquid hydrogen storage using austenitic stainless steel. In terms of elemental composition, the chemical composition of 316LN was designed based on 316 austenitic stainless steel. Quickly selecting chemical components that meet performance requirements and obtaining certification through mechanical property testing as well as determining δ-ferrite content allow us to overcome the bottleneck of time-consuming testing in multiple rounds of material preparation. Through high-throughput testing, the overall efficiency of material development has been improved by at least 10 times compared to traditional single- or few-sample preparation methods.

2 EXPERIMENTAL PART

The high-throughput preparation of components is mainly used for the study of homogeneous as-cast samples with discrete components, including also additive manufacturing method, multi-mode casting forming method, multi-crucible synchronous metallurgy method, etc. In this research, the multi-crucible synchronous metallurgy method was used to prepare as-cast samples. The experimental process included alloy sample batching, arc melting, grinding and polishing, microstructure observation, rolling, heat treatment, and mechanical-property testing. The high-throughput alloy preparation system used has a 16-station automatic arc-melting furnace, as shown in **Figure 1**. For the alloy melting process of this experiment, we adopted a high-throughput alloy preparation system, which greatly improved work efficiency by implementing multi-station automation operations in various stages of material preparation. Specifically, it eliminated the complex steps of multiple vacuum extractions required in traditional arc melting, effectively addressing the time-consuming challenge of material preparation and significantly shortening the experimental preparation and operation time for individual samples.

This investigation used pure metal block raw materials such as Ni, Cr, Mo, etc., all of which have a purity greater than 99.5 % (mass fraction), formulated according to the target alloy composition to prepare alloy samples. In a glove box filled with Ar atmosphere protection, we utilized water-cooled copper molds in an automatic arc melting furnace to achieve automatic continuous melting of pre-configured alloy blocks, thereby prepared as cast metal ingots. This workflow was ingeniously designed to melt up to 16 metal ingots at once, with each ingot weighing approximately 100 g. To ensure the uniformity of the ingot structure, we needed to repeat the melting process at least 5 times. This efficient and precise melting method significantly improved the convenience and effectiveness of our material preparation. Then, after grinding and polishing, metallographic samples were made and the ferrite content in the structure was determined using a metallographic microscope.

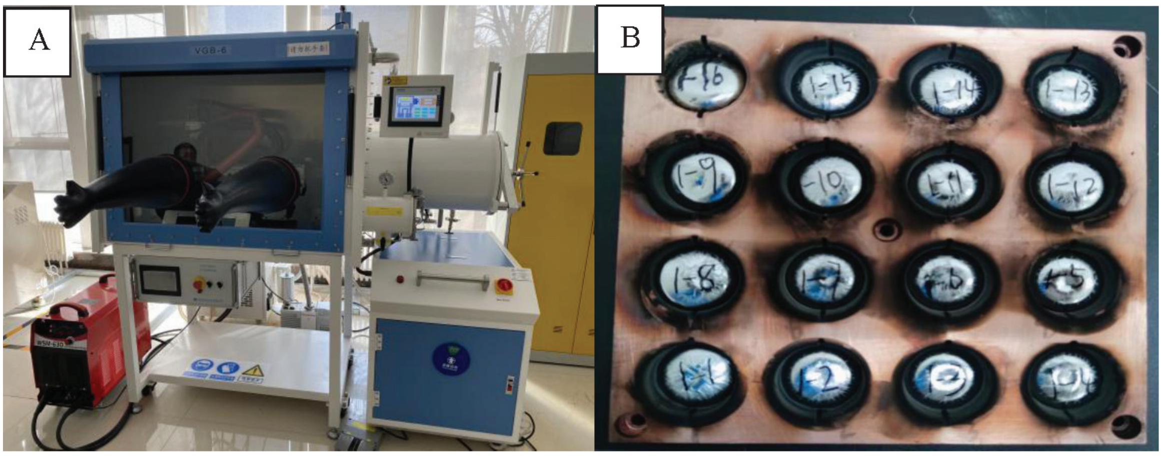

Figure 1: High-flux-material multi-crucible synchronous smelting system: a) high-throughput preparation system; b) multi-crucible synchronous metallurgical platform

3 RESULTS

Research showed that the presence of an appropriate amount of ferrite during the welding of austenitic stainless steel can reduce the tendency to hot cracking of stainless steel welds. However, when the ferrite content exceeded 3 %, it reduced the mechanical and corrosion resistance properties of the material, while increasing its sensitivity to hydrogen embrittlement, posing a safety hazard to the long-term operation of liquid hydrogen storage and transportation equipment.[3,4] Therefore, controlling the ferrite content in steel to ≤3 % became the primary principle for the composition design of 316LN austenitic stainless steel used for liquid hydrogen storage and transportation equipment. The alloy composition design strategy adopted in the first round of experiments was as follows: based on the Schaeffler phase diagram, as shown in **Figure 2**, the composition design was prepared. Random variation of the main influencing elements including nickel equivalent and chromium equivalent in the fully austenitic region resulted in the formation of four components, as shown in **Table 1**. A high-throughput preparation system was used to smelt steel ingots and determine their ferrite content, verifying the accuracy of the Schaeffler phase diagram, and preliminarily screening the chemical composition. The metallographic morphology is shown in **Figure 3.**

In theory, we can calculate the nickel equivalent and chromium equivalent of a material based on its chemical composition, and then find the corresponding microstructure and ferrite content in the phase diagram. Conversely, if we know the required microstructure composition, we can also determine the corresponding nickel equivalent and chromium equivalent values, and adjust the chemical composition of the material accordingly.[5] Although the Scheffler phase diagram considers the influence of the chemical composition on the microstructure, it does not take into account the possible effects of actual crystallization conditions and the morphology of alloy elements on the proportion of microstructure.

The results indicate that there is a certain discrepancy between the actual ferrite content and the theoretical value when using the Schaeffler diagram for composition design. Taking sample A4 as an example, the material structure with this composition is in the austenite region, with a theoretical ferrite content of 0 %, which differs from the actual content by about 9 %. Mainly due to the uniform $L \rightarrow \delta$ crystal transformation, the δ solid solution is formed. During solidification, the heat dissipation at the center of a steel ingot is relatively slow, and then the inclusion reaction occurs, $L + \delta \rightarrow g$, resulting in a decrease in δ-ferrite. However, as the temperature at the center of the steel ingot continues to decrease, the inclusion reaction ends, and some δ-ferrite is not completely transformed, thus remaining in the structure.[6] Secondly, the change in the ferrite content is determined with the solidification mode of 316LN austenitic stainless steel. The solidification mode of sample A4 prepared in the first round of high-throughput process was calculated using thermodynamic software Thermo Calc, as shown in **Figure 4**. From this figure, it can be seen that in the equilibrium state, the liquid phase of 316LN first enters a two-phase region consisting of liquid + δ-ferrite with the decreasing temperature, followed by a three-phase region of liquid + ferrite + austenite. After the liquid phase completely disappears, it goes through a solid two-phase region where ferrite and austenite coexist. In this temperature range, ferrite gradually transforms into austenite until it completely disappears at around 1290 °C: $L \rightarrow L + \delta \rightarrow L + \delta + \gamma \rightarrow \delta + \gamma$. Therefore, although the cooling rate of the steel ingot core is slow, it still exceeds 5 °C/min, a rate sufficient to reach equilibrium. The δ-ferrite formed during the high-temperature process mostly transforms into austenite during the temperature reduc-

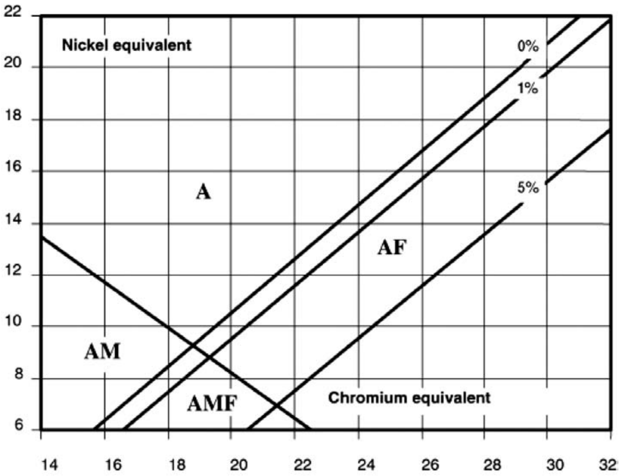

Figure 2: Schaeffler phase diagram

Table 1: Determination results for the chemical composition and ferrite content of the first round of high-flux preparation of steel ingots (wt.%)

Programme	C	Mn	Si	Cr	Ni	Mo	N	Ni$_{e}$q	Cr$_{e}$q	Ferrite≤3%	
Range	0.04–0.08	1.00–2.00	≤0.75	16.00–18.00	11.00–13.00	2.00–3.00	–	–	–	Theoretical value	Actual value
A1	0.06	1.70	0.25	16.10	12.90	2.10	0.0045	16.29	18.58	0%	4.95%
A2	0.06	1.85	0.20	16.40	12.80	2.10	0.0045	16.26	18.80	0%	5.10%
A3	0.06	1.60	0.35	16.70	11.50	2.40	0.0045	14.84	19.63	0%	8.45%
A4	0.06	1.80	0.25	17.10	11.20	2.70	0.0045	14.64	20.18	0%	9.57%

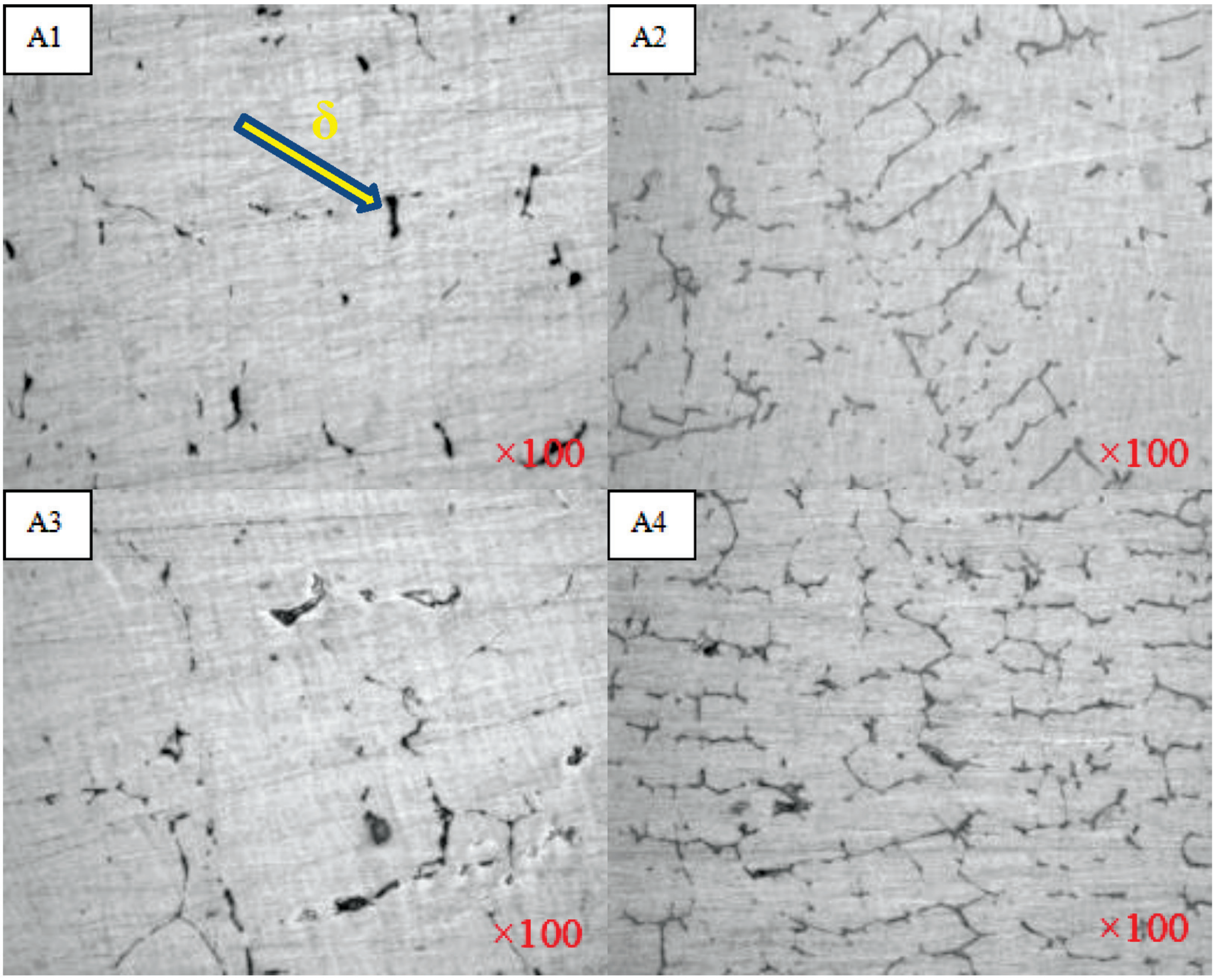

Figure 3: Metallographic photos of the ferrite content of steel ingots prepared in the first round of high flux: (A1) δ = 4.95 %; (A2) δ = 5.10 %; (A3) δ = 8.45 %; (A4) δ = 9.57 %

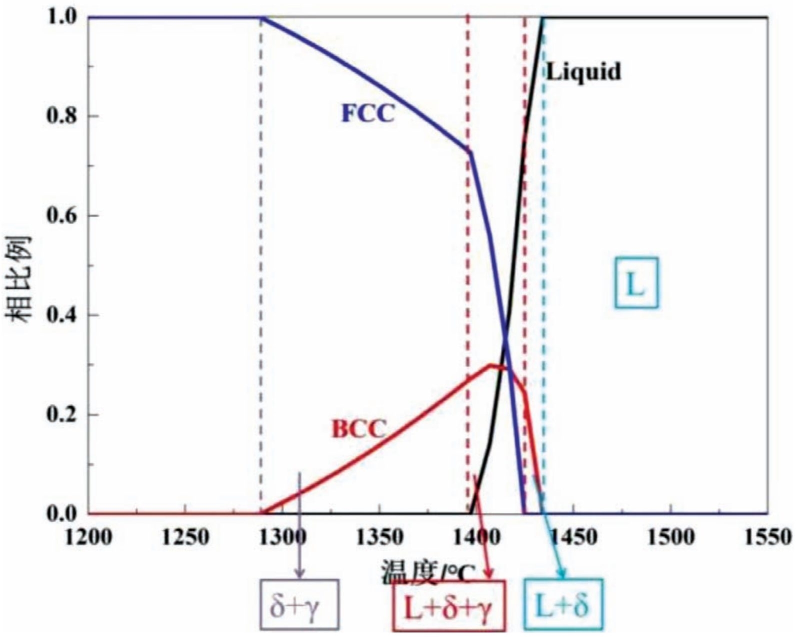

Figure 4: Solidification mode of 316LN stainless steel calculated by Thermo Calc software

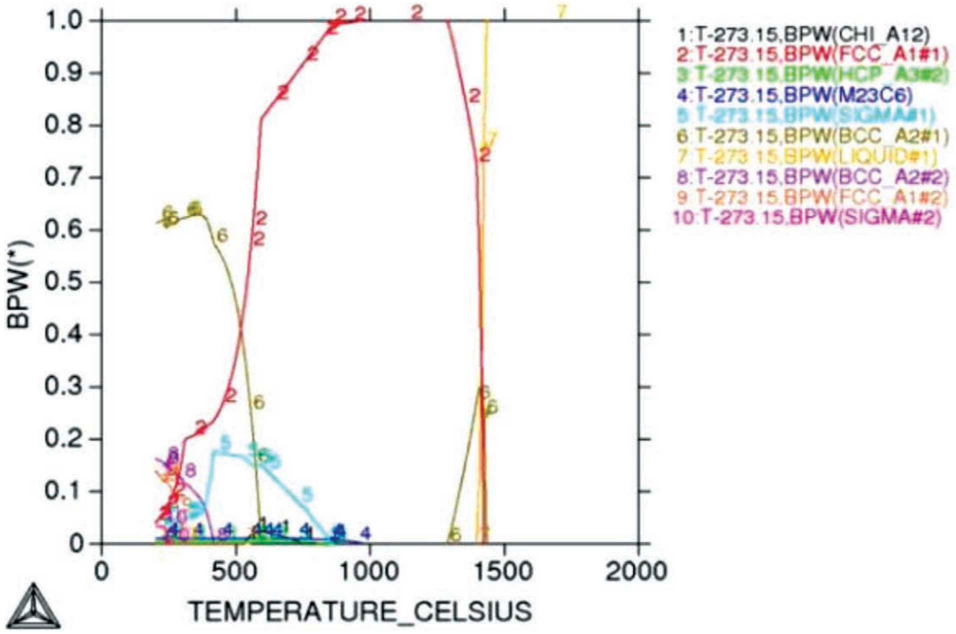

Figure 5: Equilibrium phase diagram calculated with Thermo Calc software

tion, but there is not enough time to achieve complete transformation of austenite.

In addition, the 316LN austenitic stainless steel used in this study has a high Cr content and good hardenability, indicating that the ferrite in the structure is mainly δ-ferrite, which is largely caused by component segregation. Its content can be appropriately reduced by high-temperature diffusion within the ingot or by increasing the solid solution temperature.[7,8]

A high Cr content promotes the predominance of δ-phase in ferrite through thermodynamic driving forces, solidification mode, and crystal structure compatibility. Cr, as a strong ferrite stabilizing element, preferentially forms a δ-Fe skeleton in the early stage of solidification. Its BCC structure is highly compatible with Cr atoms (lattice constant of 0.291 nm, atomic radius of 0.127 nm), having low diffusion activation energy, promoting the Cr enrichment. When 316LN stainless steel (Cr ≥ 17 %) solidifies, a high $\mathrm{Cr_e}$q shifts the solidification mode towards FA or AF, with δ-ferrite preferentially nucleating and growing as the dominant phase.

The equilibrium phase diagram of sample A4, prepared with high-throughput methods in the first round, was calculated using thermodynamic software Thermo Calc, as shown in **Figure 5**.

From **Figure 5**, it can be seen that the liquid phase (No. 7) begins to transform into δ-ferrite (No. 6) at 1430 °C. As the temperature decreases, the ferrite phase first increases to a maximum proportion of about 0.3 %, and then decreases until it disappears at 1290 °C. However, it is difficult to achieve thermodynamic equilibrium conditions in actual production. After the formation of ferrite at high temperatures, it cannot completely disappear and so it remains in the as-cast structure. The temperature range of 973–1288 °C is the single-phase austenite region. When the material undergoes high-temperature diffusion above 1230 °C, the matrix structure becomes coarse and atomic diffusion is enhanced. At this time, the reverse transformation of austenite to δ-ferrite is strengthened, resulting in a delayed dissolution of ferrite. In the later stage, with the extension of diffusion time and the migration of atoms, the composition becomes more uniform, and the metal tends to shift from non-equilibrium solidification to equilibrium state, resulting in a complete transformation of the δ-phase to the g-phase.[9] From the low-temperature section of the phase diagram, it can be seen that under thermodynamic equilibrium conditions, a portion of ferrite is also formed in this section. Starting from 584 °C, its content gradually increases with decreasing temperature to a maximum proportion of about 0.6 %. According to the phase diagram, it is impossible to completely eliminate ferrite during the smelting process. Only after adjusting the content of ferrite-forming elements (such as chromium, molybdenum, silicon, niobium, etc.) can the proportion of high-temperature ferrite be reduced.[10]

We used an electron probe to perform surface scanning of typical elements in the metallographic photo of sample A4, determining the position of ferrite. **Figure 6** shows the surface scan distribution of typical alloy elements in ferrite, grain boundaries, and austenite structures, while **Table 2** presents the energy-spectrum-analysis results for element contents at corresponding positions. From the figure, it can be seen that there is severe segregation of Mo, Cr, and Ni between the ferrite and austenite phases, with slight enrichment of C around, indicating the presence of carbides around the ferrite. According to the energy spectrum analysis in **Table 2**,

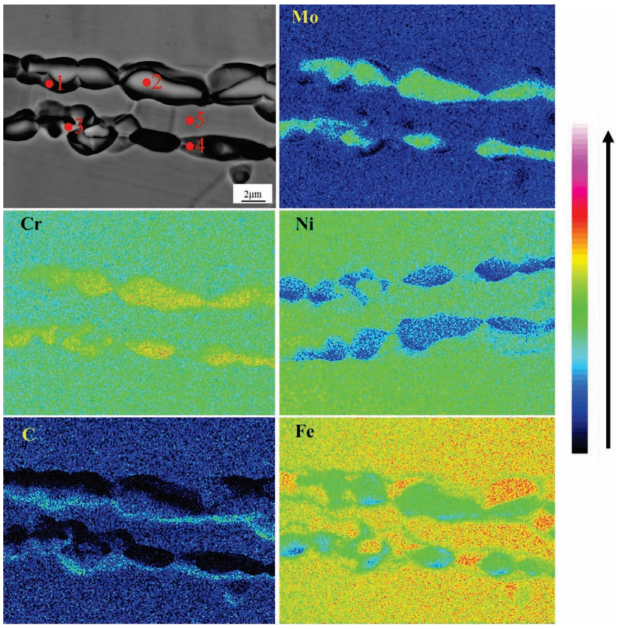

Figure 6: Plane scanning distribution of typical elements (EPMA)

the Cr content in the ferrite region reached 28.18 *w*/%, the Mo content reached 4.44 *w*/%, the Ni content decreased to 7.58 *w*/%, the C content was low, while the Cr and Mo contents in the austenite, ferrite and grain boundary structures showed an increasing trend. A stable transition of the alloy element concentration gradient indicates the formation of a compositional equilibrium zone around the ferrite. During the experiment, the steel ingot underwent structural transformation under non-equilibrium solidification conditions, resulting in regional segregation of the alloy composition. Especially, the formation elements of ferrite, such as Cr, Mo, Ni, etc., underwent severe segregation, resulting in changes in the solidification characteristics of these regions compared to the matrix material. Due to this segregation, the area of austenitization is reduced, and under the driving force of energy, structural fluctuations are generated, thereby promoting the precipitation of a large amount of δ-ferrite.[11]

Compared with Cr and Mo, Ni is a non-carbide forming element that combines with Fe to form a g solid solution. In this solution, Ni atoms replace some iron atoms and occupy their lattice positions. Due to the similar atomic radii of Ni and Fe, this substitution does not cause any significant changes in the lattice structure, ensuring the stability of the austenite structure. In addition, Ni can also affect the grain boundary structure of alloys. Ni exhibits a high solubility and can form a uniform solid solution, which helps reduce lattice distortion and stress concentration in alloys, lower the energy of grain boundaries, and hinder their migration. Ni can interact with atoms in the grain boundary region to form more stable chemical bonds, thereby optimizing the chemical composition of the grain boundary region, reducing composition segregation and precipitation formation in the alloy, which also contributes to the formation and stability of austenite phase. At the macro level, the addition of Ni can change the phase transition temperature and microstructure of the alloy. Ni can lower the temperature at which austenite transforms into other phases, allowing the austenite phase to remain stable over a wider temperature range.[12–14] In summary, the segregation of Ni element reduces the stability of austenite structure and indirectly promotes the precipitation of δ-ferrite.

This high-temperature δ-ferrite has strong stability and is difficult to dissolve during subsequent heating, rolling, and solution heat treatment processes. The traditional method is to increase the solution heat treatment temperature. With the increase on the solution temperature, the dislocation density continuously decreases and the atomic migration ability continuously increases. At the beginning, the main transformation is from the δ-phase body-centered cubic structure to the face-centered cubic g-phase. If the solution temperature is further increased to 1230 °C, the transformation from the γ-phase to the δ-phase is enhanced. This slows down the overall dissolution rate of high-temperature ferrite and causes the formation of coarse austenite grains, seriously affecting the mechanical properties and corrosion resistance of the product. Therefore, the effectiveness of solution treatment in dissolving ferrite is very limited.[15]

Table 2: EDS analysis of element composition (*w*/%)

No.	Cr	Mo	Ni	Si	Mn
1	18.99	2.93	12.31	0.25	1.82
2	**28.18**	**4.44**	**7.58**	**0.24**	**1.59**
3	19.42	3.30	11.66	0.24	1.92
4	18.56	2.99	12.07	0.27	1.79
5	16.91	2.53	13.15	0.30	1.81

Based on the above analysis, it can be concluded that the ratio of g-austenite to δ-ferrite is influenced by the combination of austenite-forming elements (such as Ni, Mn, N, etc.) and ferrite-forming elements (such as Cr, Mo, Si, etc.). The formation of δ-ferrite is mainly sensitive to the segregation of the following four elements: C, Ni, Cr, and Mo. This study intended to adjust the content of sensitive elements in a second round of experiments to identify the target chemical composition with the lowest ferrite content. The experimental plan and ferrite measurement results are shown in **Table 3**.

The results showed that the ferrite content in the metallographic structure of the B2, B3, and B7 test steel ingots was low. Heating, rolling, and solution heat treatment were carried out on the three groups of steel ingots to test the solid solution tensile properties and hot-rolled ferrite content of the test plates. The photos of the rolled test plates and the tensile specimens are shown in **Figure 7**, and the tensile and ferrite content results are shown in **Table 4**. A common feature of the three components is that the Ni, Cr, and Mo contents are controlled at mid to low levels. From the perspective of mechanical

Table 3: Chemical composition of steel ingots produced in the second round of high-flux preparation (in mass fractions (w/%))

Composition range	C 0.04 - 0.08	Si ≤ 0.75	Mn 1.00 - 2.00	P ≤ 0.03	S ≤ 0.015	Cr 16.00 - 18.00	Ni 11.00 - 13.00	Mo 2.00 - 3.00	Test plan	Ferrite≤3%	
B1	0.04	0.4	1.6	0.015	0.005	18	11	2	Scheme 1: investigate the effect of Cr on ferrite content when the content of austenite-forming elements is the lowest		5.27
B2	0.04	0.4	1.6	0.015	0.005	17	11	2			3.43
B3	0.04	0.4	1.6	0.015	0.005	16	11	2		Scheme 2: investigate the effect of Mo on ferrite content when the content of austenite-forming elements is the lowest	3.14
B4	0.04	0.4	1.6	0.015	0.005	16	11	3			6.30
B5	0.06	0.4	1.6	0.015	0.005	18	11	2	Scheme 3: investigate the effect of Cr on ferrite content at high C		7.02
B6	0.06	0.4	1.6	0.015	0.005	17	11	2			3.81
B7	0.06	0.4	1.6	0.015	0.005	16	11	2		Scheme 4: investigate the effect of Mo on ferrite content at high C	3.26
B8	0.06	0.4	1.6	0.015	0.005	16	11	3			4.07
B9	0.04	0.4	1.6	0.015	0.005	18	13	2	Scheme 5: under high Ni, the effect of Cr on ferrite content was investigated		7.26
B10	0.04	0.4	1.6	0.015	0.005	17	13	2			5.61
B11	0.04	0.4	1.6	0.015	0.005	16	13	2		Scheme 6: investigate the effect of Mo on ferrite content in the case of high Ni	4.08
B12	0.04	0.4	1.6	0.015	0.005	16	13	3			4.07
B13	0.06	0.4	1.6	0.015	0.005	18	13	2	Scheme 7: investigate the effect of Cr on ferrite content when the content of austenite-forming elements is the highest		4.05
B14	0.06	0.4	1.6	0.015	0.005	17	13	2			7.20
B15	0.06	0.4	1.6	0.015	0.005	16	13	2		Scheme 8: investigate the effect of Mo on ferrite content when the content of austenite-forming elements is the highest	4.81
B16	0.06	0.4	1.6	0.015	0.005	16	13	3			4.30

Table 4: Tensile property test results

Programme	$R_{p0.2}$/MPa	R_m/MPa	Yield ratio	*A*/%	Ferrite≤3%
Technical requirement	≥220	≥520	—	≥40	Actual value
B2	189	650	0.29	76.0	3.43
B3	217	655	0.33	73.7	3.14
B7	233	650	0.36	74.4	3.26

properties, only the B7 test plate with a higher carbon content meets the performance requirements. However, as the carbon content increases, the ferrite content in the test plate also increases. Other means must be used to optimize the alloy elements to achieve an optimal balance between mechanical properties and microstructure.

Figure 7: Photos of rolled test plates and tensile test specimens

4 DISCUSSION

There are two main methods for breaking large chunks of ferrite. One method is to crush it with low-temperature rolling with a final rolling temperature below 750 °C, and to prevent the re-enrichment of Cr and Mo during the cooling process by increasing the cooling rate after deformation.[16] The reason for using low-temperature rolling is that, firstly, the formation and stability of austenite are affected by temperature and carbon content. By reducing the rolling temperature, the transformation of austenite to ferrite can be slowed down, which helps to maintain the stability of austenite. Secondly, reducing the rolling temperature can increase deformation energy and decrease the softening rate after deformation. During the rolling process, the accumulation of deformation energy helps to increase the driving force for austenite to transform into other phases. However, as the rolling temperature decreases, deformation occurs at lower temperatures, which increases energy accumulation and enhances the system's free energy. This increase in free energy can further stabilize austenite and inhibit its transformation into other phases.[17,18]

Another method to reduce the ferrite content in austenitic stainless steel is to chemically disrupt the stability of ferrite, dividing large chunks of ferrite into granular or unstable states. For the special characteristics of 316LN stainless steel, sensitization treatment at high temperatures (around 850 °C) for extended durations can be applied. In addition, precipitation of carbides can be used to accelerate the decomposition of high-temperature ferrite. To reveal the precipitation mechanism of $M_{23}C_6$ at this temperature, the morphology of the internal δ-ferrite of a sample subjected to 15-minute short-term sensitization treatment was observed, and the results are shown in **Figure 8**. It can be seen that $M_{23}C_6$ carbides mainly precipitate at the δ/g interface during the initial sensitization stage and begins to nucleate. In addition, a small amount of residual δ-ferrite begins to transform into the σ phase in the sample. According to literature reports, the C element has an inhibitory effect on the nucleation of the σ-phase.[19] During sensitization, the precipitation of $M_{23}C_6$ carbides consumes a large amount of C atoms in the residual ferrite. When the C content decreases to a certain extent, the residual δ-ferrite can continue to undergo a transformation towards the σ phase.[20] With the precipitation of the σ phase, a large amount of solute atoms such as Cr and Mo are consumed, which makes the $M_{23}C_6$ produced during the early decomposition unstable, further transforming into secondary austenite γ 2.

Figure 9 shows the EBSD microstructure of sample B7 after hot rolling and sensitization treatment for 1 h. From the figure, it can be seen that during the slow cooling process after hot rolling, some ferrite is transformed into carbides, while after sensitization, ferrite is almost eliminated and completely transformed into carbides with a network morphology. As the sensitization progresses, the solid solubility of solute atoms such as Cr and Mo in the δ-ferrite increases significantly, and the supersaturation decreases accordingly. Therefore, the dissolution and precipitation reaction inside the ferrite grains becomes less obvious. At the same time, with the increase in the insulation time, the diffusion ability of C atoms in austenite is enhanced, and the decomposition reaction of δ-ferrite is dominated by element diffusion. At the δ/g interface, C atoms are enriched, providing favorable conditions for the nucleation of carbides. Due to the high Cr and Mo contents of δ-ferrite itself, their combination with C atoms diffusing to the interface induces the nucleation of carbides.[21] Therefore, experimental results and characterization methods demonstrated that long-term high-temperature sensitization or aging treatment can effectively destroy the as-cast microstructure and large residual ferrite content from previous processes, which is of great help in accelerating the rapid dissolution of δ-ferrite in the subsequent high-temperature solid solution heat treatment.

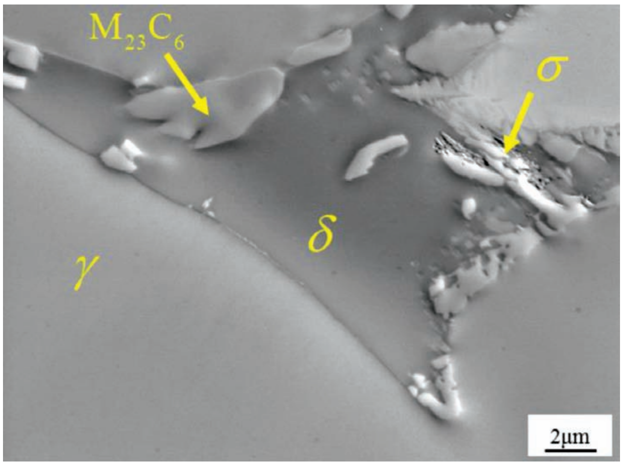

Figure 8: Microstructure of 316LN stainless steel after sensitization treatment for 15 min (EPMA)

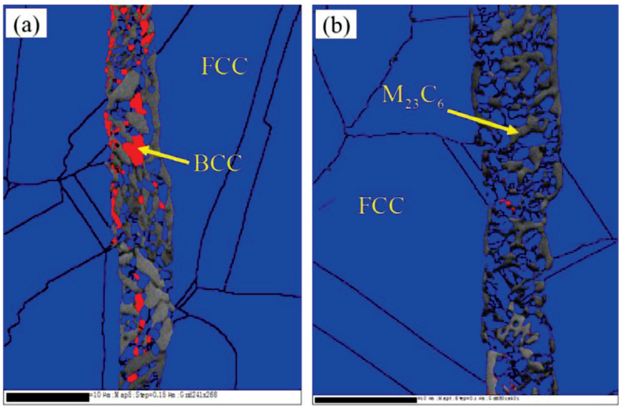

Figure 9: EBSD microstructure of hot-rolled and sensitized 316LN stainless steel: a) hot-rolled state; b) sensitization treatment and heat preservation for 1 h

Figure 10 shows the microstructure of sample B7 after sensitization treatment and solution treatment at 1060 °C. From the figure, it can be seen that the carbides were eliminated after solution treatment. After corrosion, it can be clearly seen that there is a 1.5–2 μm wide corroded and dissolved structure at the δ/g grain boundary, indicating that the corrosion resistance of δ-ferrite, austenite, and the interface between the two phases is varies, forming galvanic corrosion. The content of alloying elements in the δ-ferrite structure is high, and the electrode potential is also high. The content of alloying elements in the austenite structure is low, while the electrode potential is high. Due to the unequal electrode potential of the metal, a corrosion cell is formed, causing the electric current to flow from the high potential region to the low potential region, thereby increasing the metal dissolution rate at the interface between the two phases and causing local corrosion.

The root cause of galvanic corrosion in austenitic stainless steel lies in the difference in Fermi levels between different its internal metallic phases, leading to the generation of potential differences. The Fermi level determines the ease of electron escape, with higher Fermi levels having a stronger ability to lose electrons and lower Fermi levels having a stronger ability to gain electrons. According to solid-state physics, the intrinsic po-

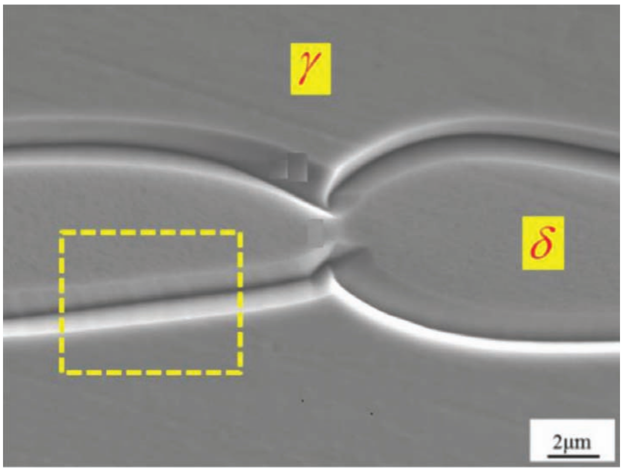

Figure 10: Microstructure of 316LN stainless steel sensitized before solid solution (EPMA)

tential difference (U γ – U δ) between the δ-phase and the austenite matrix is obtained by dividing the difference in electron work functions (W γ – W δ) by the elementary charge (e). The surface work functions of different materials are different, and materials with higher work functions have a greater difficulty releasing electrons and tend to act as cathodic phases in galvanic corrosion, making them less susceptible to corrosion. Materials with low work functions readily release electrons and act as anodes, leading to preferential corrosion. Therefore, the magnitude of the surface work function directly affects the electrochemical role and corrosion resistance of a material during corrosion; materials with lower work functions are more susceptible to corrosion.[22]

To investigate the cause of galvanic corrosion, a sample was subjected to electrolytic corrosion in a way that preserved ferrite and its surrounding microstructure; then, the corroded regions were subjected to compositional analysis. EPMA enables clear observation of the microstructure and distribution of alloy elements after electrolytic corrosion. On **Figure 11**, it can be seen that carbides with a face-centered cubic structure ($M_{23}C_6$) precipitate along the grain boundaries of austenite and ferrite. The measurement and characterization of the distribution of elements are achieved through the line scanning function of EPMA, and its energy spectrum analysis is presented in **Table 5**. From the figure and table, it can be seen that carbides rich in Cr exhibit severe precipitation at the grain boundaries between austenite and ferrite, and are distributed discontinuously in strips and blocks along these grain boundaries. At the same time, a small amount of discontinuous second phase precipitation can also be observed along the grain boundaries between austenite and the matrix. According to the data in the table, the composition of second-phase precipitates distributed along the austenite grain boundaries differ significantly from those at the austenite/ferrite grain boundaries. This is mainly reflected in the precipitation of Cr-rich carbides at the austenite/ferrite grain boundaries, while the Cr content at the austenite grain boundaries is relatively low and the Ni content is high. When the carbon content in stainless steel is high, carbon combines with chromium to form complex and unstable interstitial carbides, $M_{23}C_6$, which have an orthogonal lattice structure and strong affinity for iron, making it easy to form $(Cr, Fe)_{23}C_6$.[23] In high-temperature environments, as the temperature increases, this carbide gradually dissolves into the solid solution. If this high-temperature state is maintained at room temperature through rapid cooling, a supersaturated solid solution is formed. However, during slow cooling, carbides precipitate from the solid solution in order to maintain equilibrium. This precipitation process leads to the formation of phases rich in $M_{23}C_6$ near grain boundaries, and correspondingly, chromium-poor regions appear in austenite. Once the chromium content decreases to the minimum level required to maintain passivation, numerous microbatteries consisting of 'chromium carbide (as the cathode) and chromium depleted regions (as the anode)' form inside the steel. These microbatteries can cause corrosion in the chromium-poor areas near grain boundaries, and the larger the potential difference, the faster the corrosion rate.[24]

The precipitation of $M_{23}C_6$ at grain boundaries results in changes in the grain boundary morphology, particu-

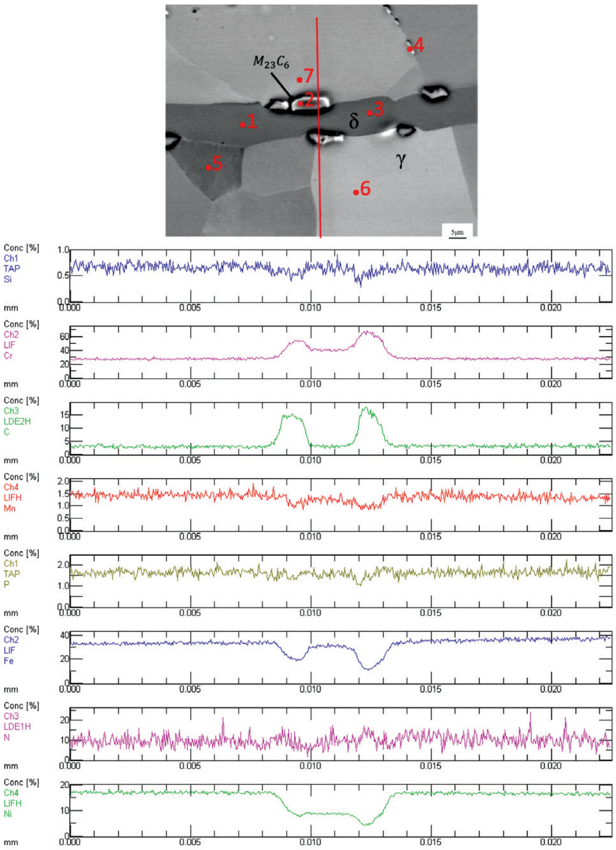

Figure 11: EPMA morphology and element distribution of 316LN stainless steel during electrolytic corrosion: a) microstructure; b) element distribution

larly the formation of pits with a width of approximately 2 μm at the δ/g grain boundaries (as shown in **Figure 10**). According to the description in reference,[25] $M_{23}C_6$ tends to preferentially precipitate at the δ/g grain boundaries, and the degree of precipitation is influenced by both the interfacial energy between the δ/g phases and the chemical driving force of the Cr element. Therefore, when the proportion of residual δ-phase is high, the number of δ/g grain boundaries also increases, providing more favorable positions for the precipitation of Cr-rich phases, thereby causing changes in the morphology of δ/g grain boundaries in austenitic stainless steel. From the analysis of the composition of the electrolytic corrosion state, it can be seen that its content and variation pattern are the same as those of the metallographic corrosion state, indicating that the interface structure of corrosion dissolution in the metallographic corrosion state is the transition zone between high Cr, Mo and low Cr, Mo components. This also proves that the potential difference caused by the segregation of precipitates and adjacent substrates is the main cause of galvanic corrosion.[26]

Table 5: EDS analysis results for element contents (*w*/%)

No.	Si	Cr	Mn	Fe	Ni
1	0.22	22.28	1.51	45.86	9.44
2	0.25	24.72	1.45	26.93	7.75
3	0.23	22.99	1.16	46.76	8.63
4	0.26	18.77	1.75	47.86	13.09
5	0.29	18.01	2.30	49.87	13.94
6	0.23	17.43	1.58	48.94	12.89
7	0.23	19.19	1.73	49.38	13.44

5 CONCLUSIONS

This study uses high-throughput experiments to accelerate the composition optimization design of 316LN austenitic stainless steel for liquid hydrogen storage and transportation equipment. Using the multi-crucible synchronous metallurgy method, stainless steel ingots with single component differences can be prepared in large quantities at multiple stations, greatly improving research and development compared to traditional single/few sample preparation processes.

The high-temperature δ-ferrite in 316LN stainless steel originates from the solidification process. Due to the redistribution of elements during solidification, Cr and Mo tend to segregate at dendrites or grain boundaries, forming Cr- and Mo-enriched regions, resulting in the nucleation and growth of ferrite. Its solidification is in the FA mode: $L \rightarrow L + \delta \rightarrow L + \delta + \gamma \rightarrow \delta + \gamma$.

Reducing the Cr$_e$q/Ni$_e$q ratio within the composition range, especially by controlling the contents of Cr and Mo, can fundamentally reduce the formation of ferrite and control its content. For a given composition, high-temperature and long-term sensitization treatment should be used to control the content of ferrite.

Under the existing process conditions, the use of high-temperature sensitization and solid solution treatment is more effective in eliminating ferrite, and can meet the requirement of δ-ferrite ≤ 3 %. A large amount of carbides forms during sensitization heat treatment. Although they contribute to ferrite decomposition, the Cr and Mo enriched in these regions exhibit limited diffusivity during subsequent solid solution heat treatment, thereby facilitating a smooth transition in Cr and Mo concentration gradient. A stable potential difference is also formed between ferrite and austenite structure and the interface of the two phase regions, forming a microbattery circuit in the electrochemical corrosion medium, thereby causing galvanic corrosion.

Acknowledgment

The authors acknowledge the support of the Fundamental Research Business Funds for Central Universities (FRF-BD-22-02).

6 REFERENCES

[1] L. Li, S. Fan, Q. Chen, et al., Research status and prospects of hydrogen storage technology, Energy Storage Science and Technology, 7 (**2018**) 4, 586–594, doi:10.12028/j.issn.2095-4239.2018.0062

[2] X. Jiang, et al., Hydrogen storage in China's hydrogen energy industry chain under the background of dual carbon, Chemical Equipment and Pipeline, 60 (**2023**) 4, 19–28

[3] R. Zhang, H. Zhu, X. Guan, et al., Effect of ferrite on properties of austenitic stainless steel, Mechanical Engineer, 60 (**2013**) 6, 41–42, doi:10.3969/j.issn.1002-2333.2013.06.018

[4] H. Yuan, et al., Study on the mechanism of ferritic susceptibility to hydrogen embrittlement of austenitic stainless steel, Boiler Technology, 53 (**2022**) 1, 48–51

[5] D. Wang, et al., Study on solidification crack sensitivity of austenitic alloy during laser welding, Rare Metal Materials and Engineering, 50 (**2021**) 7, 2436–2445, doi:10.12442/j.issn.1002-185x.20200560

[6] W. Tian, et al., Control of δ-ferrite content and austenite grain size of 0Cr16Ni5Mo martensitic stainless steel, Metal Heat Treatment, 47 (**2022**) 9, 194–201, doi:10.13251/j.issn.0254-6051.2022.09.034

[7] T. Li, Y. Li, W. Li, et al., Effect of heat treatment on properties of 0Cr16Ni5Mo stainless steel welded joints, Heat Treatment of Metals, 40 (**2015**) 11 , 120–125, doi:10.13251/j.issn.0254-6051.2015.11.028

[8] John C. Lippold, J. Damian Kotecki, Welding Metallurgy and Weldability of Stainless Steels, John Wiley & Sons, Inc., Hoboken 2005, doi:10.5860/choice.43-2230

[9] D. Zhao Dejiang, J. Pan, H. Hu, et al., Solidification properties and ferrite distribution characteristics of 316H austenitic stainless steel based on Thermo Calc calculation, Special Steel, (**2024**), doi:10.20057/j.1003-8620.2024-00245

[10] Y. Dai, X. Zheng, P. Ding, Review on sodium corrosion evolution of nuclear-grade 316 stainless steel for sodium-cooled fast reactor applications, Nuclear Engineering and Technology, 53 (**2021**) 11, 3474–3490, doi:10.1016/J.NET.2021.05.021

[11] F. Xu, et al., Effect of solution temperature on δ-ferrite transformation of 316L austenitic stainless steel, Rare Metal Materials and Engineering, 50 (**2021**) 8, 2922–2925

[12] W. Zhang, Study on strain strengthening of austenitic stainless steel cryogenic vessels, South China University of Technology, Guangzhou 2011

[13] G. Xu, F. Wang, Y. Yan, et al., Microstructure and properties of new low Ni stainless steel, Metal Heat Treatment, 39 (**2014**) 9, 92–95, doi:10.13251/j.issn.0254-6051.2014.09.024

[14] G. Xu, et al., Low temperature properties and microstructure stability of high nitrogen and low nickel austenitic stainless steel, Heat Treatment of Metals, 42 (**2017**) 2, 1–6, doi:10.13251/j.issn.0254-6051.2017.02.001

[15] Y. Wang, C. Chen, X. Yang, et al., Solidification modes and delta-ferrite of two types of 316L stainless steels: a combination of as-cast microstructure and HT-CLSM research, Journal of Iron and Steel Research International, 32 (**2025**) 2, 6880–6886, doi:10.1007/S42243-024-01401-4

[16] X. Yang, Y. Zhuang, J. Li, W. Yin, Study on grain size control of 316 austenitic stainless steel plate, Special Steel, (**2019**) 3, 70–73, doi:cnki:sun:tsga.0.2019-03-018

[17] R. Singh, D. Sachan, R. Verma, et al., Mechanical behavior of 304 austenitic stainless steel processed by cryogenic rolling, Materials Today: Proceedings, 5 (**2018**) 9, 16880–16886, doi:10.1016/j.matpr.2018.04.090

[18] X. Yang, M. Liu, Z. Liu, et al., Failure analysis of a 304 stainless steel heat exchanger in liquid sulfur recovery units, Engineering Failure Analysis, 116 (**2020**), 104729, doi:10.1016/j.engfailanal.2020.104729

[19] C. C. Hsieh, W. Wu, Overview of intermetallic sigma (σ) phase precipitation in stainless steels, International Scholarly Research Notices, (**2012**), 1–16, doi:10.5402/2012/732471

[20] G. Sasikala, S. K. Ray, S. L. Mannan, Kinetics of transformation of delta ferrite during creep in a type 316(N) stainless steel weld metal, Materials Science and Engineering: A, 359 (**2003**), 86–90, doi:10.1016/S0921-5093(03)00371-X

[21] Q. Wang, Study on the effect of δ-ferrite in nuclear grade austenitic stainless steel on related properties, University of Science and Technology of China, Hefei 2020, doi:10.27517/d.cnki.gzkju.2022.002212

[22] J. Wang, Calculation of electronic work function and its application in the study of electrochemical problems on the surface of materials, University of Science and Technology of China, Hefei 2016

[23] B. Wen, X. Chen, D. Bin, Z. Hong, et al., Effect of δ-ferrite decomposition on the tensile properties of one modified 316H stainless steel: Experimental investigations and crystal plastic finite element simulations, Materials Science and Engineering: A, 915 (**2024**), 86–90, doi:10.1016/J.MSEA.2024.147224

[24] Q. Wang, S. Chen, X. Lv, et al., Role of δ-ferrite in fatigue crack growth of AISI 316 austenitic stainless steel, Journal of Materials Science & Technology, 359 (**2022**), 9–17, doi:10.1016/J.JMST.2021.10.008

[25] B. Schluyer, G. Barkleit, F. Schneider, et al., Analysis of intergranular corrosion attack of stainless steels by means of atomic force microscopy and optical microscopy. Part 2: Influence of impurity content, Mater. Corros., 51 (**2015**) 2, 115, doi:10.1002/(SICI)1521-4176(200002)51:2<115:: AID-MACO115>3.0.CO; 2-N

[26] Z. Pang, et al., Corrosion behavior of residual δ ferrite in s31609 austenitic stainless steel, China Metallurgical, 31 (**2021)** 3, 59–65, doi:10.13228/j.boyuan.issn1006-9356.20200451